Optical palpation *in vivo*: imaging human skin lesions using mechanical contrast

Shaghayegh Es'haghian
Kelsey M. Kennedy
Peijun Gong
David D. Sampson
Robert A. McLaughlin
Brendan F. Kennedy

SPIE

Optical palpation *in vivo*: imaging human skin lesions using mechanical contrast

Shaghayegh Es'haghian,a,* Kelsey M. Kennedy,a Peijun Gong,a David D. Sampson,a,b Robert A. McLaughlin,a and Brendan F. Kennedya
aThe University of Western Australia, School of Electrical, Electronic and Computer Engineering, Optical+Biomedical Engineering Laboratory, 35 Stirling Highway, Crawley, Western Australia 6009, Australia
bThe University of Western Australia, Centre for Microscopy, Characterisation and Analysis, 35 Stirling Highway, Crawley, Western Australia 6009, Australia

Abstract. We demonstrate the first application of the recently proposed method of optical palpation to *in vivo* imaging of human skin. Optical palpation is a tactile imaging technique that probes the spatial variation of a sample's mechanical properties by producing an *en face* map of stress measured at the sample surface. This map is determined from the thickness of a translucent, compliant stress sensor placed between a loading element and the sample and is measured using optical coherence tomography. We assess the performance of optical palpation using a handheld imaging probe on skin-mimicking phantoms, and demonstrate its use on human skin lesions. Our results demonstrate the capacity of optical palpation to delineate the boundaries of lesions and to map the mechanical contrast between lesions and the surrounding normal skin. © *2015 Society of Photo-Optical Instrumentation Engineers (SPIE)* [DOI: 10.1117/1.JBO.20.1.016013]

Keywords: optical coherence tomography; optical coherence elastography; tactile imaging; optical palpation; biomechanics; skin; scar; skin lesion.

Paper 140627R received Sep. 29, 2014; accepted for publication Dec. 4, 2014; published online Jan. 14, 2015.

1 Introduction

The pathologies of skin often modify its mechanical properties. For example, scleroderma,[1,2] skin cancer,[3,4] and burn scars[5,6] all give rise to large variations in the pliability of skin. For this reason, clinicians commonly manually palpate skin lesions to obtain a subjective assessment of the pathology. In the case of burn scars, pliability, as assessed by palpation and observation, is one of the four parameters considered in the Vancouver Scar Scale, which is an assessment scale commonly used by clinicians.[7] Limitations of manual palpation include its subjectivity, low resolution, and low sensitivity. To address these limitations, a number of objective methods have been proposed to measure the mechanical properties of skin.[8,9]

Typically in such methods, the skin is subjected to a mechanical perturbation and its surface deformation, or the force required to produce a specific deformation, is measured. Examples of mechanical perturbation for *in vivo* studies include: suction,[10] compression[11] (or indentation),[12–14] torsion,[15–17] extension,[5,18,19] and acoustic wave propagation.[20] These loading mechanisms have been incorporated into a number of devices to characterize the mechanical properties of skin *in vivo*. Examples of devices that apply static or quasi-static loads orthogonal to the skin's surface include: the cutometer, which is an optical system that measures the skin surface displacement versus time under suction;[21] the tonometer, which measures the extent of depression of a plunger in a weight-loaded device placed on the skin;[11,22] and spherical indenters, which measure adhesion forces between the indenter and skin versus penetration depth by using force sensors and a motion controller to displace the indenter at a constant velocity.[13] Alternatively, some

methods utilize dynamic loading. One example is the reviscometer, which couples sound waves to skin (in the frequency range 5 to 8 kHz) and records the transit time from transmitter to receiver, with stiffer and more dense tissues having a higher sound velocity.[23] There are also methods that apply in-plane deformations such as the twistometer, which measures the skin's extensibility under torsion using a torque sensor;[24] and the quasi-static extensometer, which uses strain gauges to record the required load and apply a known rate of extension to the skin between two adhesive tabs.[19] Additionally, suction and compression loading methods have been combined with ultrasound imaging to allow the thickness of the dermis and hypodermis to be simultaneously monitored.[25–28]

Aside from the ultrasound-based approaches, these methods generally characterize the average properties of skin over regions with dimensions in the millimeter to centimeter range. Characterization of the local spatial variation of the mechanical properties of skin on the the finer submillimeter scale has the potential to aid in the assessment of a number of skin pathologies including skin cancers[29–32] and burn scars.[6]

Optical coherence elastography (OCE) has been proposed as a means of providing high-resolution images of skin stiffness.[33–38] In OCE, skin deformation is measured using optical coherence tomography (OCT). The higher resolution and higher sensitivity to sample deformation of OCE compared with the methods described above,[11,13,21–23,39–41] hold promise for detecting more subtle changes in stiffness. Several OCE approaches have been proposed for *in vivo* imaging of skin. In compression OCE, the local axial strain, defined as the rate of change of sample axial displacement versus depth, is measured in response to a compressive load on the skin surface. This technique can provide three-dimensional (3-D) strain elastograms of

*Address all correspondence to: Shaghayegh Es'haghian, E-mail: shaghayegh .eshaghian@research.uwa.edu.au

skin *in vivo*.[35] In surface acoustic wave OCE, the measured phase velocity is used to directly obtain the Young's modulus of tissue and has been demonstrated to provide quantitative, two-dimensional (2-D) elastograms of skin *in vivo*.[34,36,37]

In this paper, we present the first application of optical palpation, an OCT-based tactile imaging technique recently proposed by our group,[42] to *in vivo* imaging of skin lesions. Optical palpation is a variant of OCE in which a translucent, compliant layer acting as a stress sensor is placed between the sample and a compressive loading element. 3-D-OCT images are acquired before and after loading. The strain in the compliant layer is estimated by measuring the layer thickness using OCT. Using prior knowledge of the stress–strain behavior of the sensor material, the surface stress at each lateral location is mapped into a 2-D image. This image represents the stress at the sample surface, analogous to the stress detected by manual palpation, but at a higher spatial resolution.

To enable optical palpation to be performed *in vivo*, we have developed a handheld imaging probe to apply a compressive load to the skin while simultaneously performing OCT imaging from the same side. To assess the probe's performance, we first performed optical palpation on skin-mimicking phantoms consisting of layers mimicking the epidermis, dermis, and hypodermis. Stiff inclusions were embedded in the dermis layer to mimic a stiff lesion. Additionally, as many skin lesions feature irregular and raised surfaces, we performed optical palpation on phantoms with raised surface features to assess the impact of surface topology on measured stress. We subsequently performed optical palpation on various skin lesions from human volunteers including: a nevus, a burn scar, a scar resulting from a sutured laceration, and a hypertrophic postsurgical scar. In each case, high mechanical contrast is observed. To validate the contrast obtained, optical palpation images are compared both with corresponding OCT *en face* images and photographs. In several instances, optical palpation reveals features not visible in the corresponding OCT image.

2 Materials and Methods

2.1 *Imaging System*

Scanning was performed using a portable swept-source OCT system (OCS1300SS, Thorlabs, USA) with a central wavelength of 1325 nm and a spectral bandwidth of 100 nm. The measured axial and transverse resolutions (full-width at half-maximum) of the system are 17 μm (in air) and 16 μm, respectively. Light illuminated the sample through an objective lens with a working distance of 25 mm, delivering a scanning beam with a numerical aperture of 0.03 and a measured optical power of 4.7 mW. The dimensions (xyz) of each OCT data volume are $8 \times 8 \times 3$ mm. The system was operated at an A-scan rate of 14 kHz, and the 3-D data acquisition time was ~40 s. The OCT images presented here are normalized on a log-scale from 0 to 255 grayscale (with 0 corresponding to black and 255 corresponding to white).

2.2 *In Vivo Imaging Probe*

The handheld probe incorporates both OCT imaging and compressive loading from the same side of the sample and is an extension of OCE probes previously developed by our group.[33,35] A schematic of the probe is shown in Figs. 1(a) and 1(b), and a photograph of the probe during optical palpation imaging is shown in

Fig. 1(c). The compliant sensor is positioned between the probe and the skin. In the figure, $l_0(x, y)$ and $l(x, y)$ represent the sensor thickness before and after loading, respectively. These parameters are measured at each lateral position (x, y) by calculating the distance between the axial location of the upper and lower edges of the sensor. The edges are detected in each OCT B-scan, as the interfaces of the sensor and the bottom surface of the imaging window and skin, respectively, using a Canny edge-detector.[43] The minimum measurable sensor thickness is ~12 μm, limited by the axial resolution of the OCT system in silicone, and the maximum measurable thickness is ~2.14 mm, limited by the imaging range of the OCT system. The minimum change in sensor thickness that can be measured is determined by the axial pixel size, ~4 μm in our case. The deformation of the sensor is quantified by strain, ε, as

$$\varepsilon(x, y) = \frac{l(x, y) - l_0(x, y)}{l_0(x, y)}. \qquad (1)$$

The stress at each lateral position is then estimated from the stress–strain curve of the compliant sensor, shown in Fig. 1(d), which was independently measured using a standard compression tester (Instron, Norwood, Massachusetts). The plate of the compression tester had a diameter of 40 mm and was used to test compliant sensors with thicknesses of 1 and 3 mm and with diameters of 20 and 50 mm, respectively. Given that the minimum detectable change in sensor thickness is ~4 μm, for sensors of thickness 1 mm, the minimum measurable strain is 0.004. Assuming a sensor preload of 30%, this corresponds to a minimum detectable change in stress of ~0.3 kPa.

To provide uniform compression on the corrugated surface of the skin, the probe has a cylindrical head with an inner diameter of 10 mm and an outer diameter of 15 mm. A glass imaging window (2-mm thickness) was fixed to the base of the cylindrical head, providing optical access to the sample, as well as acting as a compression plate. The diameter of the window used in all scanning sessions, except in one, was 12.5 mm. In the session scanning the fourth skin lesion, this was replaced with a larger window of diameter 25 mm. As both of the imaging windows are larger than the area over which OCT imaging was performed (8×8 mm), and because the thickness of the compressed tissue was of the same order of magnitude as the diameter of the imaging plate, we assume that the tissue undergoes uniaxial compression, that no boundary conditions are present in the region scanned, and that no gradient in loading is introduced in the axial direction.

The length of the cylindrical head (13.5 mm), marked as L_C in Fig. 1(a), was set to maximize the probe's measurable displacement range and also the achievable axial compression in skin. Maximizing the range of displacement is of particular importance for body locations containing a thick hypodermis, the soft layer of subcutaneous fat below the skin. In this case, a larger probe displacement is required to adequately compress the epidermis and dermis. The upper limit for the length of the cylindrical head was constrained by the working distance of the objective lens (25 mm) and was set to ensure that the skin remained in focus in both pre and postcompression scans (the distance between the objective lens and the bottom surface of the imaging window could be adjusted in the range 21 to 30 mm).

Optical palpation experiments were performed with two probe configurations: a handheld setup, where the operator held the imaging probe in both the pre and postcompression acquisitions; and a configuration in which the OCT probe
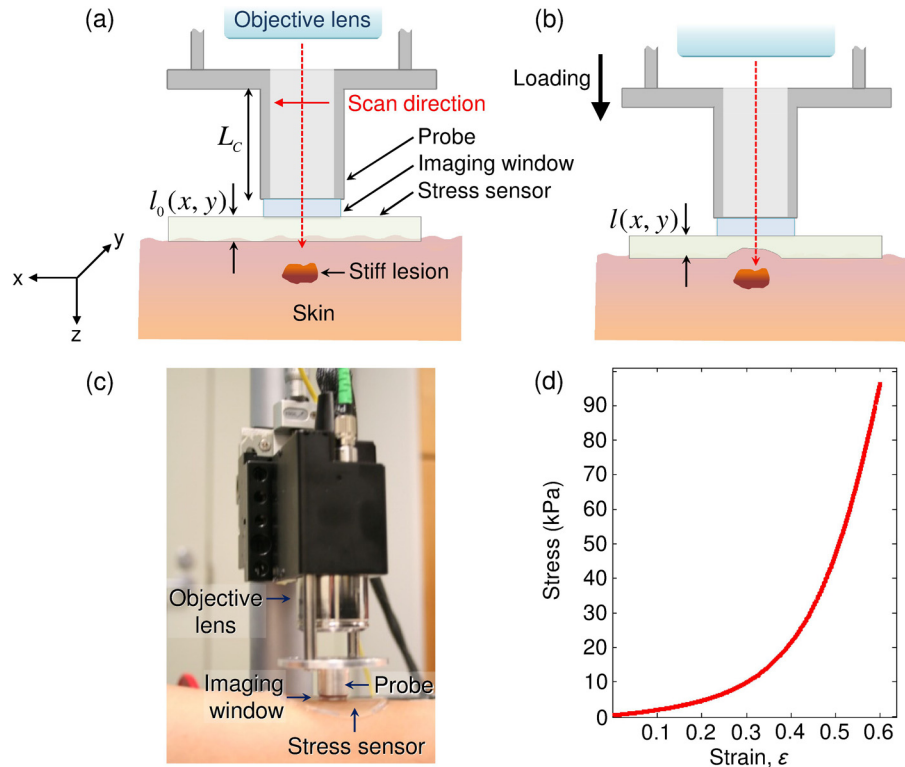
Fig. 1 *In vivo* optical palpation imaging probe: (a) and (b) schematic diagrams of the optical palpation setup for skin imaging: (a) before; and (b) after compressive loading. L_C in (a) represents the length of the cylindrical head of the probe. $l_0(x, y)$ in (a) and $l(x, y)$ in (b) represent the local sensor thickness before and after loading, respectively. (c) Photograph of the probe, demonstrating optical palpation on skin *in vivo*. (d) Representative stress–strain curve of the sensor material, used to estimate the local stress from the measured local strain.

was fixed to a translation stage to allow well-controlled compression of the sample. In the latter configuration, the translation stage was either fixed to a stand, as shown in Fig. 1(c), or installed on an articulating arm, similar to one used by our group previously for OCT skin imaging.[44]

2.3 Stress Sensor

The translucent stress sensors were fabricated with a thickness of 1 mm and a diameter of 50 mm using Elastosil® P7676 and AK50 Silicone Fluid (Wacker, Germany), as described in detail previously.[45] The mechanical properties of these compliant silicone materials can be controlled by altering the ratios of silicone catalyst, cross-linker, and non-cross-linked silicone fluid.

Because optical palpation measures the sensor deformation in order to determine stress, a key requirement is that the sensor stiffness is such that it deforms when compressed against skin. The sensors used here have a Young's modulus in the range 7 to 21 kPa. This range matches well with the range previously reported for skin stiffness.[12,14,46,47]

2.4 Optical Palpation on Skin-Mimicking Phantoms

To assess the performance of our imaging setup, skin-mimicking phantoms were fabricated using combinations of silicone elastomers similar to those used in the fabrication of stress sensors and, additionally, Elastosil® RT601 (Wacker). The optical properties of the phantoms were controlled by adding titanium dioxide (TiO_2) particles to the silicone mixture prior to adding the

silicone cross-linker.[45] The Young's modulus of each material used in the phantoms was independently measured using a standard compression tester (Instron). We performed optical palpation on phantoms with the probe fixed to a translation stage which was attached to a stand. The stress sensors used in these experiments have a Young's modulus of 19 kPa.

Two three-layer phantoms, illustrated in Fig. 2, were fabricated with optical, mechanical, and structural properties mimicking those of human skin. The superficial layer (Layer A) has Young's modulus of 120 kPa and thickness of 200 μm, mimicking the epidermis. The thickness of this layer is in the range of the epidermal thickness of human skin, which varies from $\sim 30 - 150\,\mu$m for thin skin up to $\sim 500 - 800\,\mu$m for thick skin.[48,49] The softer middle layer (Layer B) has Young's modulus of 12 kPa and thickness of 1.7 mm, mimicking the dermis. This layer contains inclusions with Young's modulus of 120 kPa and approximate dimensions (xyz) of $1 \times 1 \times 0.7\ mm$ to mimic stiff lesions, such as intradermal lipomas.[50] The inclusions were embedded such that they extend in depth to $\sim 0.5\ mm$ above the top of Layer C. The deepest, softest layer (Layer C) is 2-mm thick with Young's modulus of 5 kPa, mimicking the hypodermis.

In Phantom 1, the embedded inclusion has a higher concentration of TiO_2 scatterers (1.5 mg/mL) than in the substrate (0.5 mg/mL), providing optical contrast between the inclusion and the substrate. In Phantom 2, the inclusion has the same concentration of scatterers as in the substrate (0.5 mg/mL), resulting in negligible optical contrast between the inclusion and Layer B in the OCT image. The concentration of scatterers is
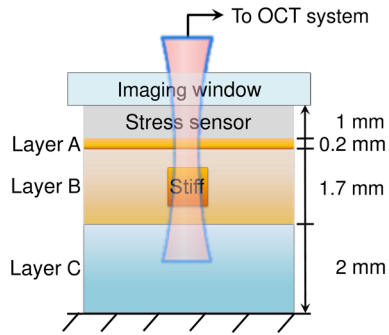
Fig. 2 Schematic diagram of the structure of the skin-mimicking Phantoms 1 and 2. The three layers in the phantoms mimic the mechanical properties of the epidermis, dermis, and hypodermis, respectively. The stiff inclusion in Phantom 1 has higher scattering than the surrounding layer, while in Phantom 2, it has scattering matched to that of the surrounding layer. The approximate dimensions (xyz) of the inclusions are $1 \times 1 \times 0.7$ mm, and the thickness of the stress sensor and the layers of the phantom are marked at right.

1.5 mg/mL in Layer A, making this layer distinguishable from Layer B. Optical palpation was performed on these phantoms by applying a 2-mm compression between scans.

To assess the performance of optical palpation on uneven surfaces, we fabricated two silicone phantoms with raised surface features. In Phantom 3, we fabricated a raised feature with higher stiffness (300 kPa) than the substrate (18 kPa). In Phantom 4, we fabricated a raised feature with the same stiffness (18 kPa) as the substrate. The raised features are cylindrical, with a diameter of 1 mm and length of >5 mm and are parallel to and partially embedded $200\,\mu$m beneath the surface of the phantom, creating a rounded ridge on the surface, as seen in Figs. 5(a) and 5(b). In both phantoms, the thickness of the substrate, marked as L in Figs. 5(a) and 5(b), is $\sim2.6\,mm$ and the concentration of TiO_2 scatterers is 0.8 mg/mL throughout. Optical palpation was performed by bringing the probe into full contact with the phantom surface. A minimal preload was applied to the sensor over the raised features, just

sufficient to ensure that the probe was in full contact with the sensor in the precompression scans. The preload was set by observing, using OCT imaging, the contact between the window of the probe and the sensor immediately prior to loading and image acquisition. The postcompression scans were acquired after applying an additional displacement of 1.1 mm, which corresponds to 30% bulk strain on the system, including the 1-mm sensor and the phantom.

2.5 Optical Palpation on Skin Lesions

Optical palpation was carried out *in vivo* on volunteers (Caucasian, two males and one female, mean age 32) with skin lesions on the dorsal forearm, the wrist, the dorsal hand, and the ventral arm. The lesions were a nevus and three scars resulting from a burn, a sutured laceration, and a surgical excision, respectively. In each case and prior to imaging, photographs of the imaging location were taken and the skin lesion and the adjacent normal skin were marked for 3-D-OCT imaging. Hair on the imaging location was trimmed using an electric shaver prior to scanning to reduce shadowing artifacts in OCT imaging. To minimize friction, the skin and both sides of the stress sensor were lubricated with silicone fluid before positioning the sensor on the skin surface. After positioning the sensor, the imaging probe was brought into full contact with the sensor. Prior to 3-D-OCT acquisition in the unloaded case, it was verified by visual inspection of OCT B-scans that potential sources of artifact, such as compression at an angle or trapped oil, were not present. To minimize compression and motion artifacts, the limb being scanned was supported using sand bags. After acquiring the unloaded 3-D-OCT dataset, the imaging probe was lowered to increase the compression in both the sensor and the skin. In the loaded case, the same procedure was adopted: several OCT B-scans were visually inspected to verify the absence of artifacts. In the processing routine, if a noticeable lateral shift between the OCT scans before and after compression was observed, a landmark in the image, such as a hair follicle, was used to laterally coregister the scans prior to estimating the axial strain in the sensor. In the results presented,
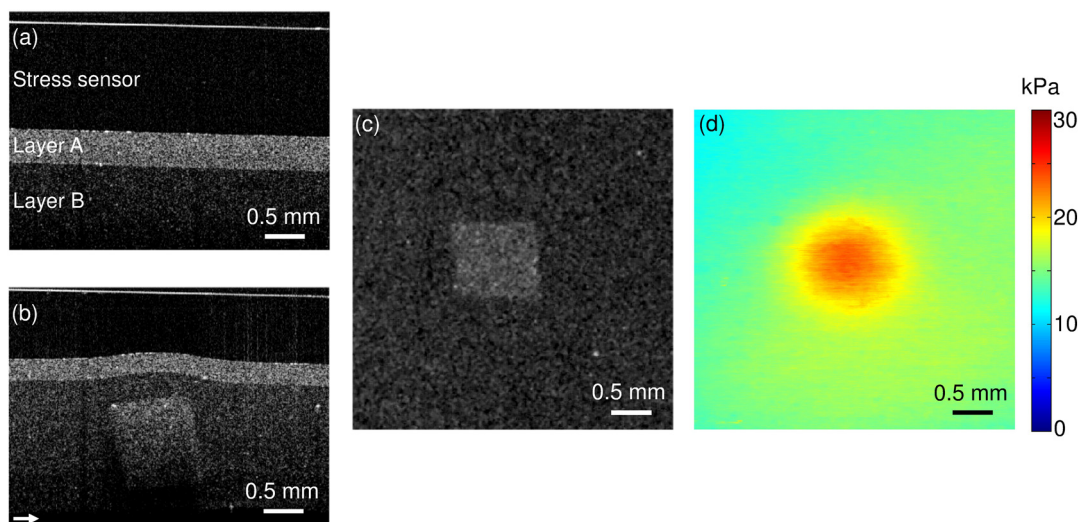

Fig. 3 Phantom 1: (a) and (b) OCT B-scans acquired from the central region of the phantom before and after compression, respectively. The arrow in (b) indicates the top section of Layer C. (c) *En face* OCT image after compression, 580 μm beyond the interface of the sensor and Layer A. (d) Corresponding stress map.
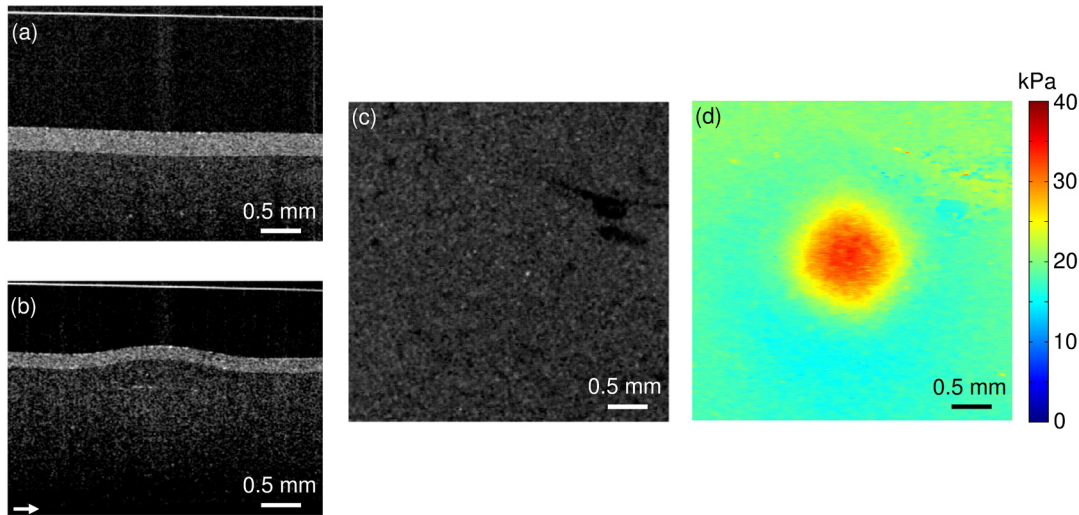
Fig. 4 Phantom 2, in which the optical properties of the embedded stiff inclusion match the surrounding silicone matrix. (a) and (b) OCT B-scans acquired from the central region of the phantom before and after compression, respectively. The arrow in (b) indicates the top section of Layer C. (c) *En face* OCT image after compression, 840 μm beyond the interface between the sensor and the phantom surface, cutting through the center of the stiff inclusion. (d) Corresponding stress map.

the depth of the *en face* OCT image plane beneath the sample surface is reported as a physical length, assuming an average group refractive index of 1.4 for silicone and 1.43 for skin.[51]

3 Results

3.1 Tissue Phantoms

3.1.1 Phantoms 1 and 2: three layers with "dermal" inclusions

Figure 3 shows the results of optical palpation on a portion of Phantom 1 that contains a stiff inclusion in the "dermis" layer. Figures 3(a) and 3(b) show representative OCT B-scan images before and after loading, respectively. In these B-scans, the specular reflection close to the top of the image is caused by the bottom surface of the imaging window. The stress sensor lies below this surface, appearing as a region of very low scattering between the imaging window and the phantom. The superficial layer of Phantom 1, Layer A, appears as a high scattering layer above the less scattering middle layer in which the inclusions are embedded. In the unloaded image, the penetration depth of OCT does not reach the location of the inclusion [Fig. 3(a)], but this inclusion comes fully into the B-scan field-of-view after compression [Fig. 3(b)]. Also in Fig. 3(b), Layer C comes slightly into the field-of-view, appearing as a dark band below the moderately scattering Layer B [indicated by the arrow in Fig. 3(b)].

As seen in Fig. 3(b), the stress sensor is compressed more over the stiff inclusion (mean strain ∼43%) than over the rest of the substrate (mean strain ∼34%). The 2-D *en face* map of stress is shown in Fig. 3(d), illustrating the mechanical contrast between the inclusion and substrate. The mean stress above the inclusion is ∼22 kPa, compared with ∼14 kPa in the rest of the phantom. This result demonstrates the ability of optical palpation to detect mechanical contrast in a phantom mimicking a stiff lesion in the dermis. Figure 3(c) shows an *en face* OCT image, taken from a physical depth of 580 μm beyond the interface of the sensor and Layer A. Comparing the OCT image with the stress map [Fig. 3(d)] confirms that the variation in

mechanical contrast matches the apparent lateral location of the stiff inclusion. The spatial resolution of optical palpation will be discussed below in Sec. 4.

To demonstrate the independence of mechanical and optical contrast, Fig. 4 shows the results of optical palpation on Phantom 2, which has the same structural and mechanical properties as Phantom 1 but contains an inclusion with optical properties matched to those of Layer B. Thus, the inclusion is not visible in the OCT image. Figures 4(a) and 4(b) show representative OCT B-scan images before and after compression, respectively.

The response of the stress sensor in Fig. 4(b) is similar to that in Fig. 3(b); a higher axial deformation (∼45% mean strain) is observed above the stiff inclusion compared with the soft surrounding material (∼38% mean strain). Figure 4(c) shows an *en face* OCT image of Phantom 2 after compression at a physical distance 840 μm beyond the interface of the sensor and the phantom surface. This *en face* plane cuts through the center of the stiff inclusion; however, the inclusion is not visible as it has the same optical properties as the surrounding layer. The stress map, shown in Fig. 4(d), provides high contrast between the inclusion (∼30 kPa mean stress) and the soft surrounding material (∼17 kPa mean stress). This experiment demonstrates that optical palpation can detect features independently of the optical contrast of the sample. This result also suggests that optical palpation could provide contrast complementary to that provided by OCT if the variations in optical and mechanical contrast were to be different for a given feature.

3.1.2 Phantoms 3 and 4: phantoms with raised surface features

Figure 5(c) shows the result of optical palpation on a portion of Phantom 3 containing a stiff, raised feature. This stress map provides high contrast between the region above the raised feature (∼22 kPa mean stress) and the rest of the phantom (∼13 kPa mean stress). To validate that the higher stress above the raised feature resulted from its higher stiffness and not as an artifact of its raised topology, Fig. 5(d) shows the result of optical
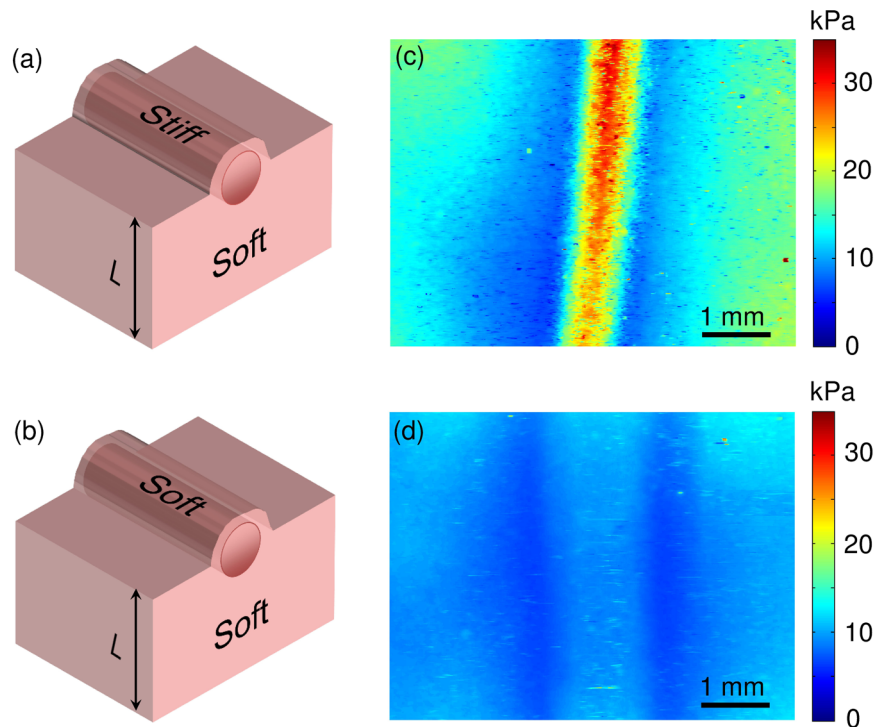
Fig. 5 Optical palpation on phantoms with a raised surface feature. (a) and (b) Schematic diagrams of the imaged portion of Phantoms 3 and 4, respectively, in which a silicone cylinder with diameter of 1 mm was partially embedded 200 μm below the surface of the phantom. *L*, the thickness, is ~2.6 mm. (c) and (d) Corresponding stress maps of Phantoms 3 and 4, respectively.

palpation on a portion of Phantom 4, containing the raised feature with the same stiffness as the rest of the phantom. In Fig. 5(d), the mean stress of the raised feature (~9 kPa) is close to that of the remainder of the phantom (~9.8 kPa).

The results of optical palpation on Phantoms 3 and 4 indicate that, first, mechanical contrast between a stiff raised feature at the surface and the rest of a sample is readily observable and that, second, the raised topology of surface features does not lead to overestimation of the stress over a raised feature.

In the stress maps presented in Figs. 5(c) and 5(d), two parallel regions of lower stress are visible at the left and right sides of the raised features. These regions appear due to the incompressibility of the sensor material, which links the axial compression with lateral expansion in order to preserve volume. The lateral expansion of the sensor in the regions adjacent to the raised features leads to lower axial strain and, therefore, lower stress than in regions far from the raised features.

3.2 Optical Palpation on Skin Lesions

In this section, we demonstrate the contrast provided by *in vivo* optical palpation on skin lesions from volunteer subjects. In each case, a photograph, *en face* OCT image and stress map are presented. The representative *en face* OCT image was chosen from the 3-D volume so as to maximize the contrast between the lesion and the surrounding skin.

3.2.1 Subject 1: nevus

To demonstrate optical palpation *in vivo* on a clearly delineated feature, we scanned a nevus (diameter ~2 mm) on the dorsal forearm. The nevus, shown in the photograph in Fig. 6(a), is dark, slightly raised, and under manual palpation felt stiffer than the surrounding tissue. Figure 6(b) shows an *en face* OCT image in the unloaded case, 200 μm beyond the interface of the sensor and the skin surface, in which the nevus appears as
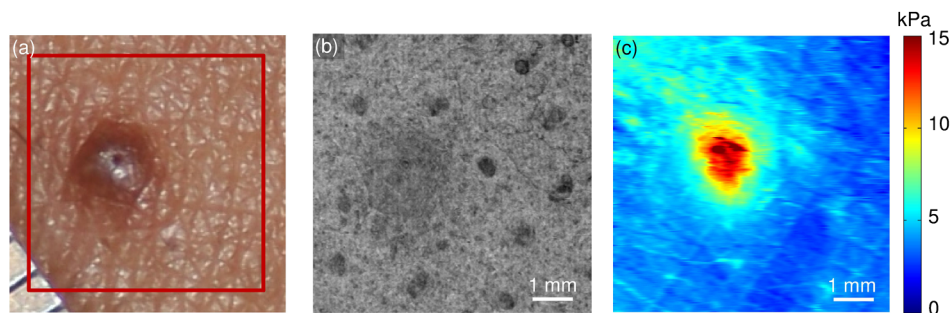

Fig. 6 Subject 1: nevus on the dorsal forearm. (a) Photograph of the region imaged. The red rectangle corresponds to the field-of-view in (b) and (c). (b) *En face* OCT image before compression, 200 μm beyond the interface of the sensor and the skin surface. (c) Corresponding stress map of the skin lesion.
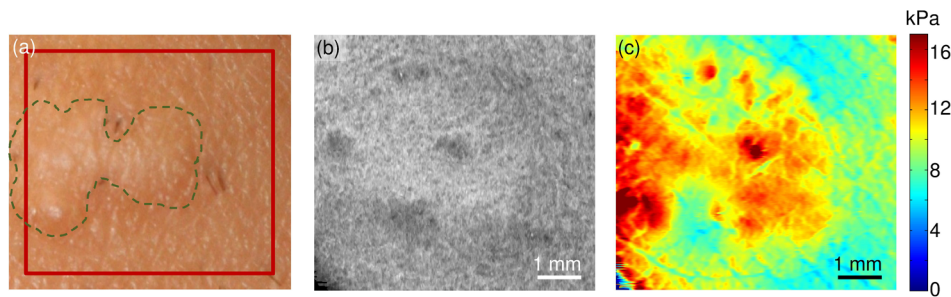
Fig. 7 Subject 2: a burn scar on the wrist. (a) Photograph of the region imaged. The dashed green line delineates the scar. The red rectangle corresponds to the field-of-view in (b) and (c). (b) *En face* OCT image before compression, 200 μm beyond the interface of the sensor and the skin surface. (c) Corresponding stress map.

a slightly darker region (lower signal), most likely caused by melanin. The dark, oval-shaped regions around the nevus of diameter <0.3 mm are hair follicles in cross-section.

Optical palpation was performed on this nevus in a handheld configuration in which the operator held the probe over the imaging location. For stability, the arm of the operator was supported on a cushion and located close to the imaging location. Using a stress sensor with Young's modulus of 21 kPa, the stress map in Fig. 6(c) is obtained, in which high mechanical contrast is provided between the lesion (~12 kPa mean stress) and the surrounding skin (~4 kPa mean stress). Comparing Figs. 6(b) and 6(c), we note that the border of the nevus is more clearly delineated in the stress map than in the *en face* OCT image.

3.2.2 *Subject 2: burn scar*

In Fig. 7, we demonstrate optical palpation on a burn scar resulting from a scald with hot oil on the wrist above the radius bone. This lesion, shown in Fig. 7(a), is mature (>10-year-old), slightly raised, and stiffer to the touch than the surrounding tissue. The lesion was imaged with the probe fixed to a translation stage, which was affixed to a stand. Figure 7(b) shows an *en face* OCT image in the unloaded configuration, 200 μm beyond the interface of the sensor and the skin surface. The OCT intensity is slightly higher in the scarred region. A displacement of 2.6 mm was applied between the unloaded and loaded scans. The acquired stress map in Fig. 7(c) shows: higher stress over the burn scar than over the surrounding skin; clearer delineation of the scar than the corresponding *en face* OCT image [Fig. 7(b)]; and heterogeneity of mechanical properties distributed throughout the lesion.

3.2.3 *Subject 3: suture scar*

To demonstrate optical palpation on a flat lesion, we imaged a portion of a mature scar (>10-year-old) resulting from a sutured laceration, shown in Fig. 8(a), on the dorsal hand of a volunteer. Notably, variations in mechanical properties between the scar and surrounding tissue were sufficiently subtle that, by palpating the lesion manually with a fingertip, it was not possible to distinguish the scar from the surrounding skin. To acquire this scan, we used an articulating arm to facilitate uniaxial compression of the imaging region and applied a 1.5-mm probe displacement between the unloaded and loaded scans. Figure 8(c) shows the stress map, which readily differentiates the scar region from the surrounding skin. The stress map corresponds well to the photograph in Fig. 8(a), delineating the region of scarring. Such contrast is not present in the *en face* OCT image, shown in Fig. 8(b), which corresponds to a depth of 330 μm beyond the interface of the sensor and the skin surface.

3.2.4 *Subject 4: hypertrophic scar due to surgical excision*

Figure 9 shows the results from a mature (~3-year-old) hypertrophic scar on the ventral arm of a volunteer, formed as a result of surgical excision. The scarred region was stiff and raised due to an overproduction of collagen characteristic of hypertrophic scarring. Microvasculature imaging, performed using a speckle decorrelation technique,[44] revealed a prolific network of blood vessels present, which is also characteristic of hypertrophic scarring.

As this nodular scar, shown in Fig. 9(a), had a diameter comparable with the probe head, it was challenging to place the
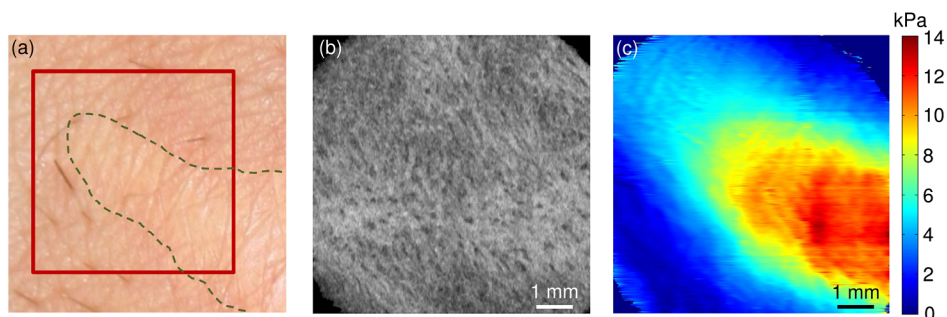

Fig. 8 Subject 3: a scar caused by a sutured laceration on the dorsal hand. (a) Photograph of the region imaged. The dashed green line delineates the scar. The red rectangle corresponds to the field-of-view in (b) and (c). (b) *En face* OCT image before compression, 330 μm beyond the interface of the sensor and the skin surface. (c) Corresponding stress map.
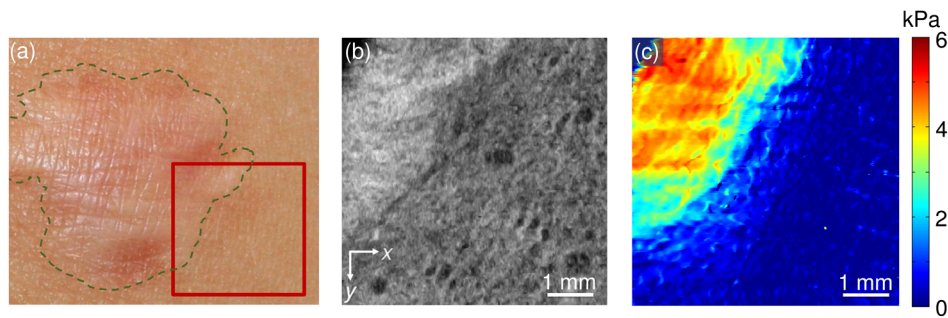
Fig. 9 Subject 4: a hypertrophic scar caused by surgical excision on the ventral arm. (a) Photograph of the imaging location. The dashed green line delineates the scar. The red rectangle corresponds to the field-of-view in (b) and (c). (b) *En face* OCT image after compression, 270 μm beyond the interface of the sensor and the skin surface. (c) Corresponding stress map.

probe such that both the scar and adjacent skin were compressed. To overcome this, the 12.5-mm diameter imaging window was replaced by a larger window of diameter 25 mm. To perform imaging, we used a softer stress sensor (Young's modulus 14 kPa) to account for the thicker layer of subcutaneous fat at this imaging location. Using the articulating arm, the compression angle of the probe was adjusted to be parallel to the plane of the skin-scar surface, and the probe was displaced by ∼12 mm. Figure 9(b) shows an *en face* OCT image in the compressed case, 270 μm beyond the interface of the sensor and the skin surface. As the scar was elevated, there was a lateral shift between the OCT scans acquired before and after compression: 1.4 and 1.54 mm shifts away from the fast and slow scanning directions, respectively, shown in Fig. 9(b) as x and y arrows. The pre and postcompression OCT scans were manually co-registered in the lateral direction prior to calculating the strain.

The stress map is shown in Fig. 9(c) and demonstrates high mechanical contrast between the scar region in the top left of the image and the adjacent skin. The region of high stress in Fig. 9(c) corresponds well with the scar region in the photograph in Fig. 9(a) and the *en face* OCT image in Fig. 9(b), in which the scar appears as a region with a slightly higher OCT signal in the top left.

4 Discussion

The results presented here demonstrate the ability of optical palpation to provide mechanical contrast between lesions and the surrounding skin, which exceeds that available from OCT imaging alone. An advantage of optical palpation over many OCE techniques for imaging mechanical contrast *in vivo* is that phase-sensitive detection is not required, placing less stringent requirements on the OCT system. Additionally, as optical palpation is derived from the OCT signal in the stress sensor, it can be used to map the mechanical properties of even very opaque tissue.

The use of a compliant layer enables this technique to provide useful measurements when the skin surface is uneven, as its conformity to the surface topography allows sufficiently uniform stress to be applied across the sample surface. This feature is highlighted by the results on the phantoms with raised features and in three of the *in vivo* results, where the imaged lesions had raised and irregular surfaces.

In this study, we aimed to probe mechanical contrast produced within the epidermis and dermis. As the tissue beneath the dermis, such as the hypodermis and bone, also influences the contrast in optical palpation, several steps were taken to minimize its influence. First, we found that the presence of a thick layer of hypodermis required significantly higher displacements

of the imaging probe before the mechanical contrast in the superficial layers of skin could be observed. If the hypodermis was insufficiently loaded, then we observed bulk motion of the sensor during loading, as the hypodermis compressed in preference to the stiffer superficial layers, precluding our ability to measure stress. To achieve mechanical contrast from the dermis also required this layer to compress in the loaded state. To meet these two demands, we fabricated sensors with stiffness intermediate between that expected of the dermis and hypodermis, allowing both layers to be compressed. Underlying bone also influences the contrast in optical palpation. In particular, an uneven distribution of bone within the region under compression introduces a gradient in stress that is largely independent of the mechanical properties of the superficial skin layers. To mitigate this effect, we chose the smallest probe size that provided both sufficiently uniform loading and an adequate imaging field-of-view. Gradients in stress also result from the probe and the underlying bone not being parallel. Consequently, an important aspect of the imaging protocol involved careful alignment of the probe to the skin surface, as described in Sec. 2.5.

As part of our imaging protocol, during the probe displacement and while performing imaging, volunteers were asked to report any pain or discomfort. Additionally, the operator used real-time feedback of the sensor compression observed in OCT B-scans as an indicator to avoid overloading the tissue. During image acquisition, we utilized the minimum probe displacement necessary to produce strain contrast in the sensor. For cases in which very high skin compression is needed to produce contrast, the stress observed in the stress–strain curves of the sensors at 70% strain (the highest strain level characterized) is less than 205 kPa. This level of stress is below the reported pain threshold for humans (0.4 MPa)[52] and far below the reported pain tolerance values (∼0.5 − 1.1 MPa).[22,52–55] In the results presented here, the measured stress was always <20 kPa.

The lateral resolution of optical palpation has previously been reported to be 180 μm.[42] This measurement was obtained using a phantom comprising a column of soft silicone, with Young's modulus 20 kPa, adjacent to a column of stiffer silicone, with Young's modulus of 4 MPa. While this measurement is to some extent representative of the lateral resolution in optical palpation imaging of skin *in vivo*, it is important to note that the resolution is dependent not only on that of the optical imaging system, but also on the structural and mechanical heterogeneities within the sample and, consequently, is likely to vary for different skin regions. For the phantoms used in this study, using the technique reported previously,[42] we measured lateral resolutions in the range 160 to 390 μm. The measured values

correspond to the 10% to 90% spatial "step" response of the stress at the interface of the inclusion and the adjacent phantom matrix. Insight into the variation in lateral resolution can be gained by considering the different geometries and mechanical contrasts in the phantoms reported here. In particular, phantoms 1 and 2 demonstrate how feature geometry can impact the lateral resolution in optical palpation. In these phantoms, the axial thickness of the inclusions is small compared with the overall phantom thickness (Fig. 2), and consequently, the edges of the inclusions are blurred in the stress maps [Figs. 3(d) and 4(d)]. The resolution of optical palpation is also linked with the compressibility of the material used in the stress sensor. We have used soft silicone sensors with Poisson's ratio of ~0.5 (nearly incompressible), which signifies that the axial compression in the sensor is accompanied by lateral expansion, which also contributes to blurring of the feature boundaries detected. Further studies incorporating models of skin deformation are required to rigorously assess the variation in resolution caused by the presence of heterogeneity within skin.

The lateral resolution reported here (160 to 390 μm) for optical palpation on skin-mimicking phantoms is much higher than that of methods which record the mechanical behavior of skin by averaging it over the region being probed: including the cutometer (2 mm),[21] tonometer (1 mm),[22] twistometer (3 mm),[24] and indentation testers (2 to ~6 mm).[13,56] There is scope to improve the lateral resolution toward that of the underlying OCT resolution by using inverse methods. Such methods have been proposed in related tactile imaging techniques.[57]

In the 2-D stress map in Fig. 6(c), we note additional structures caused by the skin microrelief. Skin microrelief refers to the fine intersecting lines on the outermost layer of skin, which are visible in Fig. 6(a). This contrast does not arise from higher or lower stress in the sensor; rather, it arises from a limitation of our edge-detection algorithm in accurately detecting the bottom surface of the sensor. The skin microrelief restricts the stress sensor from making full contact with the skin. As the OCT signal from the interface of air and skin is stronger than that from the interface of the sensor and air, our algorithm detects the former interface rather than the latter. One means to remove this small artifact could be to add a thin, high-scattering layer of silicone to the sensor surface that is in contact with the sample and to estimate the thickness of the sensor as that of the low-scattering region. Using spin coating techniques, it may be possible to make very thin (<10 μm) layers for this purpose.

The results on phantoms presented here demonstrate that optical palpation can tolerate surface unevenness comparable with that found in skin. Further studies are required to establish the degree of unevenness that may be tolerated. Additionally, optical palpation on skin *in vivo* could potentially be extended to provide quantitative measurements of elasticity by calculating the strain in the tissue, i.e., by combining optical palpation with compression OCE.[39,42]

5 Conclusion

Assessing the mechanical properties of skin at submillimeter spatial resolution has great potential to aid in the assessment of a number of skin pathologies. In this paper, we presented the first demonstration of optical palpation on human skin *in vivo*, which probes the mechanical properties of skin by measuring the local stress imparted to a compliant sensor placed on the skin surface. Our *in vivo* imaging probe was first validated on skin-mimicking phantoms, demonstrating the mechanical

contrast of a lesion embedded in the artificial dermis layer and confirming that the stress maps provide useful mechanical contrast even in the presence of irregular surface topology. Our *in vivo* results on a range of human skin lesions demonstrate the ability of this technique to provide high spatial resolution and mechanical contrast, enabling submillimeter delineation of the borders of stiff lesions and providing additional contrast compared with the corresponding 3-D-OCT image.

References

1. G. E. Pierard and C. M. Lapière, "Physiopathological variations in the mechanical properties of skin," *Arch. Dermatol. Res.* **260**(3), 231–239 (1977).
2. B. Kalis et al., "In vivo study of scleroderma by non-invasive techniques," *Br. J. Dermatol.* **122**(6), 785–791 (1990).
3. J. S. Moon and C. H. Oh, "Solar damage in skin tumors: quantification of elastotic material," *Dermatology* **202**(4), 289–292 (2001).
4. Y. Nishimori et al., "Degenerative alterations of dermal collagen fiber bundles in photodamaged human skin and UV-irradiated hairless mouse skin: possible effect on decreasing skin mechanical properties and appearance of wrinkles," *J. Invest. Dermatol.* **117**(6), 1458–1463 (2001).
5. J. A. Clark et al., "Mechanical characterization of human postburn hypertrophic skin during pressure therapy," *J. Biomech.* **20**(4), 397–406 (1987).
6. C. A. Grant, P. C. Twigg, and D. J. Tobin, "Static and dynamic nanomechanical properties of human skin tissue using atomic force microscopy: effect of scarring in the upper dermis," *Acta Biomater.* **8**(11), 4123–4129 (2012).
7. Z. Tyack et al., "A systematic review of the quality of burn scar rating scales for clinical and research use," *Burns* **38**(1), 6–18 (2012).
8. C. Edwards and R. Marks, "Evaluation of biomechanical properties of human skin," *Clin. Dermatol.* **13**(4), 375–380 (1995).
9. N. Brusselaers et al., "Burn scar assessment: a systematic review of objective scar assessment tools," *Burns* **36**(8), 1157–1164 (2010).
10. S. S. L. Fong, L. K. Hung, and J. C. Y. Cheng, "The cutometer and ultrasonography in the assessment of postburn hypertrophic scar—a preliminary study," *Burns* **23**, S12–S18 (1997).
11. I. Lye et al., "Tissue tonometry is a simple, objective measure for pliability of burn scar: is it reliable?" *J. Burn Care Res.* **27**(1), 82–85 (2006).
12. A. Delalleau et al., "Characterization of the mechanical properties of skin by inverse analysis combined with the indentation test," *J. Biomech.* **39**(9), 1603–1610 (2006).
13. C. Pailler-Mattei and H. Zahouani, "Analysis of adhesive behaviour of human skin in vivo by an indentation test," *Tribol. Int.* **39**(1), 12–21 (2006).
14. C. Pailler-Mattei et al., "In vivo skin biophysical behaviour and surface topography as a function of ageing," *J. Mech. Behav. Biomed.* **28**, 474–483 (2013).
15. R. Sanders, "Torsional elasticity of human skin in vivo," *Pflug. Arch. Eur. J. Phys.* **342**(3), 255–260 (1973).
16. P. G. Agache et al., "Mechanical properties and Young's modulus of human skin in vivo," *Arch. Dermatol. Res.* **269**(3), 221–232 (1980).

17. E. Berardesca et al., "In vivo biophysical characterization of skin physiological differences in races," *Dermatologica* **182**(2), 89–93 (1991).
18. T. Sugihara et al., "The extensibility in human skin: variation according to age and site," *Br. J. Plast. Surg.* **44**(6), 418–422 (1991).
19. J. A. Clark, J. C. Y. Cheng, and K. S. Leung, "Mechanical properties of normal skin and hypertrophic scars," *Burns* **22**(6), 443–446 (1996).
20. D. L. Bader and P. Bowker, "Mechanical characteristics of skin and underlying tissues in vivo," *Biomaterials* **4**(4), 305–308 (1983).
21. S. S. Fong, L. K. Hung, and J. C. Cheng, "The cutometer and ultrasonography in the assessment of postburn hypertrophic scar—a preliminary study," *Burns* **23**(Suppl 1), S12–S18 (1997).
22. G. F. Corica et al., "Objective measurement of scarring by multiple assessors: is the tissue tonometer a reliable option?," *J. Burn Care Res.* **27**(4), 520–523 (2006).
23. A. A. McHugh et al., "Biomechanical alterations in normal skin and hypertrophic scar after thermal injury," *J. Burn Care Rehabil.* **18**(2), 104–108 (1997).
24. C. Escoffier et al., "Age-related mechanical properties of human skin: an in vivo study," *J. Invest. Dermatol.* **93**(3), 353–357 (1989).
25. S. Diridollou et al., "In vivo model of the mechanical properties of the human skin under suction," *Skin Res. Technol.* **6**(4), 214–221 (2000).
26. F. M. Hendriks et al., "A numerical-experimental method to characterize the non-linear mechanical behaviour of human skin," *Skin Res. Technol.* **9**(3), 274–283 (2003).
27. S. Diridollou et al., "An in vivo method for measuring the mechanical properties of the skin using ultrasound," *Ultrasound Med. Biol.* **24**(2), 215–224 (1998).
28. J. C. M. Lau, C. W. P. Li-Tsang, and Y. P. Zheng, "Application of tissue ultrasound palpation system (TUPS) in objective scar evaluation," *Burns* **31**(4), 445–452 (2005).
29. T. Hinz et al., "Real-time tissue elastography as promising diagnostic tool for diagnosis of lymph node metastases in patients with malignant melanoma: a prospective single-center experience," *Dermatology* **226**(1), 81–90 (2013).
30. S. Aoyagi et al., "Usefulness of real-time tissue elastography for detecting lymph-node metastases in squamous cell carcinoma," *Clin. Exp. Dermatol.* **34**(8), E744–E747 (2009).
31. S. J. Kirkpatrick et al., "Imaging the mechanical stiffness of skin lesions by in vivo acousto-optical elastography," *Opt. Express* **14**(21), 9770–9779 (2006).
32. J. D. Krehbiel et al., "Digital image correlation for improved detection of basal cell carcinoma," *Exp. Mech.* **50**(6), 813–824 (2010).
33. B. F. Kennedy et al., "In vivo dynamic optical coherence elastography using a ring actuator," *Opt. Express* **17**(24), 21762–21772 (2009).
34. X. Liang and S. A. Boppart, "Biomechanical properties of in vivo human skin from dynamic optical coherence elastography," *IEEE Trans. Biomed.* **57**(4), 953–959 (2010).
35. B. F. Kennedy et al., "In vivo three-dimensional optical coherence elastography," *Opt. Express* **19**(7), 6623–6634 (2011).
36. C. H. Li et al., "Determining elastic properties of skin by measuring surface waves from an impulse mechanical stimulus using phase-sensitive optical coherence tomography," *J. R. Soc., Interface* **9**(70), 831–841 (2012).
37. C. H. Li et al., "Quantitative elastography provided by surface acoustic waves measured by phase-sensitive optical coherence tomography," *Opt. Lett.* **37**(4), 722–724 (2012).
38. C. Li et al., "Laser induced surface acoustic wave combined with phase sensitive optical coherence tomography for superficial tissue characterization: a solution for practical application," *Biomed. Opt. Express* **5**(5), 1403–1419 (2014).
39. B. F. Kennedy, K. M. Kennedy, and D. D. Sampson, "A review of optical coherence elastography: fundamentals, techniques and prospects," *IEEE J. Sel. Top. Quantum Electron.* **20**(2), 7101217 (2014).
40. C. R. Sun, B. Standish, and V. X. D. Yang, "Optical coherence elastography: current status and future applications," *J. Biomed. Opt.* **16**(4), 43001 (2011).
41. L. A. Matveev et al., "Novel methods for elasticity characterization using optical coherence tomography: brief review and future prospects," *Photonics Lasers Med.* **3**(4), 295–309 (2014).
42. K. M. Kennedy et al., "Optical palpation: optical coherence tomography-based tactile imaging using a compliant sensor," *Opt. Lett.* **39**(10), 3014–3017 (2014).
43. J. Canny, "A computational approach to edge-detection," *IEEE Trans. Pattern Anal. Mach. Intell.* **PAMI-8**(6), 679–698 (1986).
44. Y. M. Liew et al., "In vivo assessment of human burn scars through automated quantification of vascularity using optical coherence tomography," *J. Biomed. Opt.* **18**(6), 061213 (2013).
45. G. Lamouche et al., "Review of tissue simulating phantoms with controllable optical, mechanical and structural properties for use in optical coherence tomography," *Biomed. Opt. Express* **3**(6), 1381–1398 (2012).
46. C. Pailler-Mattei, S. Bec, and H. Zahouani, "In vivo measurements of the elastic mechanical properties of human skin by indentation tests," *Med. Eng. Phys.* **30**(5), 599–606 (2008).
47. J. T. Iivarinen et al., "Experimental and computational analysis of soft tissue stiffness in forearm using a manual indentation device," *Med. Eng. Phys.* **33**(10), 1245–1253 (2011).
48. Y. Lee and K. Hwang, "Skin thickness of Korean adults," *Surg. Radiol. Anat.* **24**(3–4), 183–189 (2002).
49. J. T. Whitton and J. D. Everall, "The thickness of the epidermis," *Br. J. Dermatol.* **89**(5), 467–476 (1973).
50. C. A. French et al., "Intradermal spindle cell/pleomorphic lipoma - a distinct subset," *Am. J. Dermatopathol.* **22**(6), 496–502 (2000).
51. T. Gambichler et al., "In vivo data of epidermal thickness evaluated by optical coherence tomography: effects of age, gender, skin type, and anatomic site," *J. Dermatol. Sci.* **44**(3), 145–152 (2006).
52. G. Pickering et al., "Impact of age, gender and cognitive functioning on pain perception," *Gerontology* **48**(2), 112–118 (2002).
53. W. C. Lee, M. Zhang, and A. F. Mak, "Regional differences in pain threshold and tolerance of the transtibial residual limb: including the effects of age and interface material," *Arch. Phys. Med. Rehab.* **86**(4), 641–649 (2005).
54. A. A. Fischer, "Pressure algometry over normal muscles. Standard values, validity and reproducibility of pressure threshold," *Pain* **30**(1), 115–126 (1987).
55. A. Izquierdo-Roman et al., "Mechanical tissue optical clearing technique increases imaging resolution and contrast through ex vivo porcine skin (vol 43, pg 814, 2011)," *Laser Surg. Med.* **43**(10), 998–1007 (2011).
56. G. Boyer et al., "Dynamic indentation on human skin in vivo: ageing effects," *Skin Res. Technol.* **15**(1), 55–67 (2009).
57. V. Egorov and A. P. Sarvazyan, "Mechanical imaging of the breast," *IEEE Trans. Med. Imaging* **27**(9), 1275–1287 (2008).

Shaghayegh Es'haghian is a PhD student in the Optical+Biomedical Engineering Laboratory, The University of Western Australia. She received the M.Sc. degree in biomedical engineering from University of Tehran, Iran, in 2011. Working on spatial pattern analysis of brain activity, she completed a research program at University of Rostock, Germany, in 2010. Her research focuses currently on the development of in vivo optical techniques for imaging the mechanical properties and microstructures of skin tissue.

Kelsey M. Kennedy is currently completing a PhD in the Optical+Biomedical Engineering Laboratory, The University of Western Australia. She received the B.Sc. degree in mechanical engineering from the University of Notre Dame, Indiana, in 2010. Her research focuses on the development of optical techniques for imaging the mechanical properties of tissues.

Peijun Gong is a PhD student in the Optical+Biomedical Engineering Laboratory, The University of Western Australia. He received his B.Eng. degree in electronic science and technology from Shandong University in 2009. His current research interests include the application of optical coherence tomography to disease assessment, with a focus on assessing tissue birefringence and optical attenuation.

David D. Sampson heads the Optical+Biomedical Engineering Laboratory in the School of Electrical, Electronic & Computer Engineering, The University of Western Australia, and is director of the Centre for Microscopy, Characterisation & Analysis, which is The University of Western Australia's microimaging core facility, and a node of the Australian Microscopy & Microanalysis Research Facility and the

(Australian) National Imaging Facility. He is an SPIE Fellow, OSA Fellow, and Senior Member of the IEEE. His personal research interests are in optics and photonics applied to medicine and biology.

Robert A. McLaughlin is an associate professor at The University of Western Australia. After 3 years as a postdoctoral researcher at The University of Oxford, he spent 5 years in the medical imaging industry, developing several products to commercial release. He returned to The University of Western Australia in 2007, where he now leads research into the development of miniaturized fiber-optic probes for cancer imaging, and quantitative techniques for assessment of skin using optical coherence tomography.

Brendan F. Kennedy received his PhD in the area of optical communications systems from Dublin City University, Ireland, in 2006. From 2006 to 2007, he was employed as a lecturer at the University of Santiago, Chile. Since 2008, he has worked in the Optical+Biomedical Engineering Laboratory at the University of Western Australia. His principal research interest is optical elastography.